



Bioderived ether design for low soot emission and high reactivity transport fuels

Journal:	<i>Sustainable Energy & Fuels</i>
Manuscript ID	SE-ART-03-2022-000293.R1
Article Type:	Paper
Date Submitted by the Author:	29-Jun-2022
Complete List of Authors:	<p>Cho, Jaeyoung; National Renewable Energy Laboratory Kim, Yeonjoon; National Renewable Energy Laboratory Etz, Brian; National Renewable Energy Laboratory Fioroni, Gina; National Renewable Energy Laboratory Naser, Nimal; National Renewable Energy Laboratory Zhu, Junqing; Yale University, Chemical and Environmental Engineering Xiang, Zhanhong; Yale University, Chemical and Environmental Engineering Hays, Cameron; National Renewable Energy Laboratory Alegre-Requena, Juan V.; Colorado State University St. John, Peter; National Renewable Energy Laboratory, Biosciences Center Zigler, Bradley; National Renewable Energy Laboratory McEnally, Charles; Yale University, Chemical and Environmental Engineering Pfefferle, Lisa; Yale University, Chemical and Environmental Engineering McCormick, Robert; National Renewable Energy Laboratory Kim, Seonah; Colorado State University, Chemistry; National Renewable Energy Laboratory</p>

ARTICLE

Bioderived ether design for low soot emission and high reactivity transport fuels

Received 00th January 20xx,
Accepted 00th January 20xx

DOI: 10.1039/x0xx00000x

Jaeyoung Cho^{a,†}, Yeonjoon Kim^{b,†}, Brian D. Etz^a, Gina M. Fioroni^a, Nimal Naser^a, Junqing Zhu^c, Zhanhong Xiang^c, Cameron Hays^a, Juan V. Alegre-Requena^b, Peter C. St John^a, Bradley T. Zigler^a, Charles S. McEnally^c, Lisa D. Pfefferle^c, Robert L. McCormick^a, Seonah Kim^{a,b,*}

Bioderived ethers have recently drawn attention as a response to increasing demands on clean alternative fuels. A theory-experiment combined approach was introduced for the five ether molecules representing linear, branched, and cyclic ethers to derive rational design principles for low-emission and high-reactivity ethers. Flow reactor experiments and quantum-mechanical calculations were performed at high- (750–1100K) and low-temperature (400–700K) regimes to investigate the structural effects on their sooting tendency and reactivity, respectively. At high-temperatures, ethers' high-sooting tendency is related to increased C₃ and C₄ hydrocarbon formation compared to C₁ and C₂ products from oxidation reactions. On the other hand, the reactivity at the low-temperature regime is determined by the activation energies of reaction steps leading to ketohydroperoxide formation. These studies found that ethers' sooting tendency and reactivity are relevant to two structural factors: the carbon type (primary to quaternary) and the relative position of ether oxygen atoms to carbon atoms. These factors were utilized to build a multivariate regression model, fitted to the cetane number (CN) and yield sooting index (YSI) of 50 different ethers. The model suggests building blocks with specific carbon types that maximize CN and minimize YSI, leading to design principles for ethers having low-emissions and high-reactivity as fuels for transport applications. Ethers with a high CN and low YSI were then proposed using the developed model, and through experimental measurements, it was demonstrated that they are promising biodiesel candidates.

Introduction

Concerns over pollutant emissions from combustion devices such as internal combustion (IC) engines and gas turbine have driven research on cleaner combustion strategies and emission control catalysts.^{1–4} Additionally, the need to reduce greenhouse gas emissions has led to the study of biofuels as alternatives to petroleum-derived fuels^{5–7}. Among various biofuels, low-net carbon emitting ethers in the diesel boiling range can be produced from biomass by various pathways.^{8–10} They have favorable properties for use in engines, potentially enhancing performance and lowering tailpipe emissions.¹¹ For example, the International Council on Clean Transportation recognized the bioderived dimethyl ether as a promising fuel candidate for reducing emissions from ships by 23 – 58 %.¹² A recent study⁸ suggested a novel production process of C₁₁ ethers from lignocellulosic biomass, which can be realized with a minimum fuel selling price of \$2.56 per gasoline gallon equivalent in the best scenario.

To rationally design (bioderived) ethers with improved properties, there have been experimental and computational studies on the combustion kinetics of C₂–C₈ linear^{13–21} and

branched ethers.^{22–25} These studies give insights into the oxidation chemistry and provide kinetic models for combustion simulations. Recent studies on cyclic ethers emphasize dioxolane as a promising alternative fuel prepared from biomass upgrading processes.²⁶ Several researchers have reported fuel properties of dioxolanes, highlighting that they are desirable bio-derived diesel candidates^{27–29} with low-soot emission and moderate reactivity, and the detailed kinetic mechanism of the simplest dioxolane was proposed by Wildenberg et al.²⁹

Comprehensive studies encompassing various cyclic and acyclic ethers on a consistent basis are needed to elucidate the chemical structural effects on emissions and reactivity. Yield sooting index (YSI) and cetane number (CN) have been widely used as standardized metrics for characterizing the sooting tendency and the auto-ignition delay of fuels, respectively. YSI³⁰ is proportional to the soot concentration in the co-flow diffusion methane flame doped with test fuels, which is accepted as a useful indicator of particulate matter emission from practical combustion devices^{31,32}. The CN³³ is correlated with the auto-ignition delay in the conventional compression-ignition (CI) engines; still, it effectively describes the combustion characteristics of other combustion devices, such as the heat release rate of advanced CI engine³⁴ and the lean blowout of turbojet engine.³⁵

However, they have rarely been considered together when screening biofuel candidates. **Figure 1A** and **1B** summarize experimental values of YSI and CN for a broad range of ethers. As shown, various types of ethers have been considered as an alternative fuel, including linear/branched ethers, oxetane,

^a Fuels & Combustion Science, National Renewable Energy Laboratory

^b Department of Chemistry, Colorado State University

^c Department of Chemical and Environmental Engineering, Yale University

[†] Electronic Supplementary Information (ESI) available: Detailed reaction pathway of soot precursor formation, the energetics of low-temperature chemistry, the C-H bond dissociation energy of test fuels, YSI & CN database of 50 ether compounds. See DOI: 10.1039/x0xx00000x

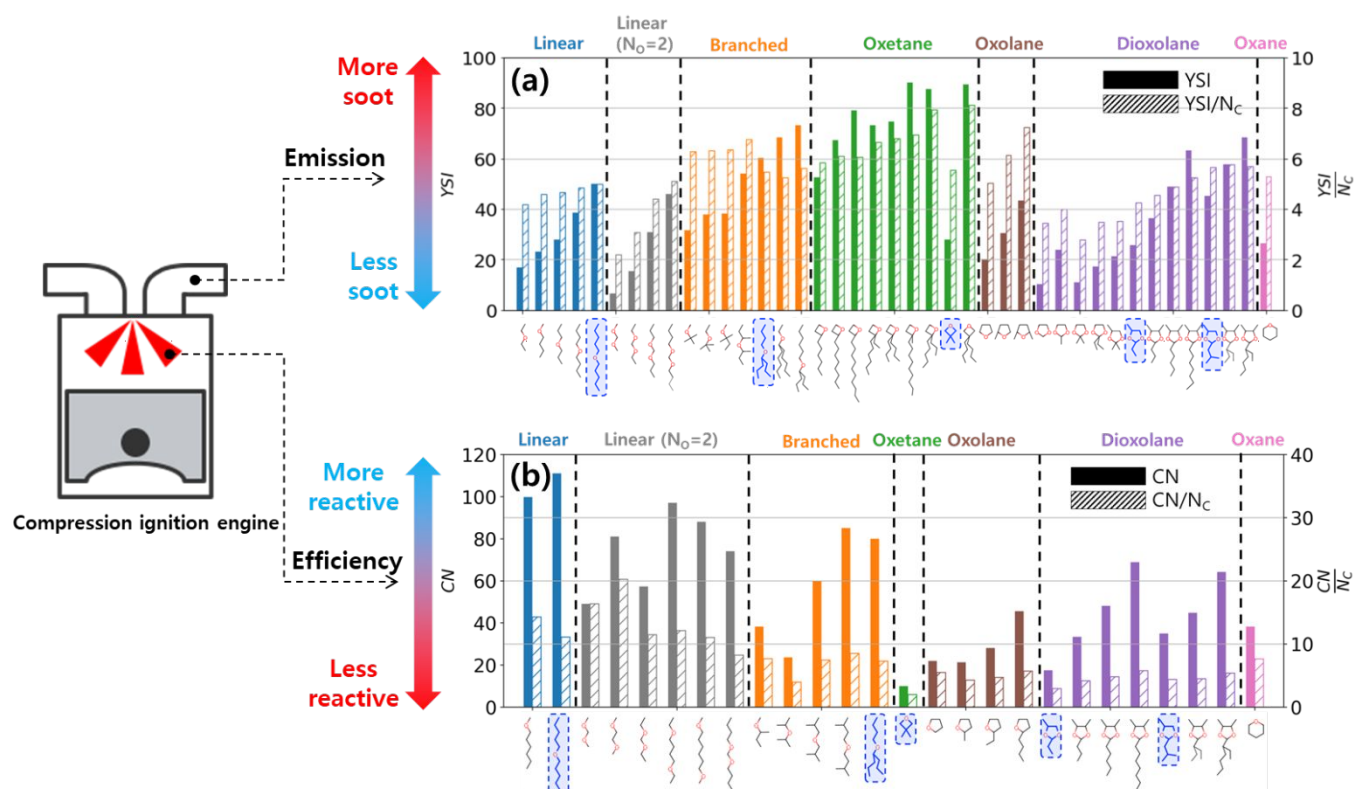


Figure 1. Structural effect of ethers on the (A) sooting tendency measured as YSI and (B) reactivity measured as CN. All the YSI and CN values were based on the experimental data from the literature and this study. The normalized values of YSI and CN to N_c were also depicted aside. The five molecules analyzed in this study are highlighted in blue.

oxolane, dioxolane, and oxane. Their YSI and CN do not monotonically correlate with the number of carbons (N_c), showing the importance of several structural features such as carbon type (primary to quaternary), the existence of a ring, number, and position of oxygens. In other words, **Fig. 1** highlights the importance of a thorough understanding of the effect of fuel structure on the YSI and CN, facilitating a guideline to design alternative fuels with low-soot emissions and high-reactivity.

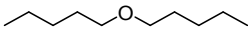
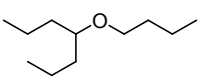
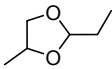
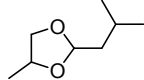
In this study, we investigate the combustion chemistry of saturated linear, branched, and cyclic ethers to rationalize how the chemical structure affects ethers' sooting tendency and reactivity. Five fuels representing various structural features of ethers were selected (**Table 1**), and the products from their oxidation at low- (400 – 700 K) to high- (750 – 1100 K) temperature chemistry regimes were identified using a flow reactor experiment. Mechanistic studies using quantum mechanics (QM) calculations and multivariate linear regression revealed a relationship between the fuel chemical structure and the product speciation. One conventional way of analyzing combustion kinetics is to develop a detailed kinetics model, run a kinetics simulation, and validate it to the experimental data. However, the mechanistic studies of this paper provide only a skeletal reaction pathway to elucidate how each molecular feature in ethers affects the YSI and CN. This holistic analysis only gave a qualitative explanation of the experimental observation. Still, it led us to identify the important molecular features for developing the multivariate model, which eventually guided the model for rational design of biofuel in the

last section. We believe that further study on the detailed kinetics of various ether molecules should be followed to enable the quantitative prediction of combustion characteristics. However, it requires a significant contribution from theoretical and experimental research.

It should be emphasized that the selected molecules listed in **Table 1** are renewable diesel fuel candidates that can potentially be produced from biomass. Saturated linear and branched ethers can be produced in large quantities from catalytic Guerbet coupling and dehydration of bioderived alcohols.⁸⁻¹⁰ About 62% yield of C_8 - C_{16} diesel-range ethers was achieved and maintained for 400 hours of time-on-stream operation when 10-50 μ l/min of ethanol was fed to catalytic reactors.⁹ Specifically for 4-butoxyheptane, more than 700 g was produced from the 16 hours' time-on-stream catalytic upgrading of butyrate obtained by *Clostridium butyricum* fermentation of corn stover.⁸ Cyclic ethers include dioxolane and oxetane. Dioxolanes can be produced via the catalytic reaction between diols and methyl ketones, both of which are made from the fermentation of biomass sugars. The catalytic efficiency can be significantly enhanced under mild reaction conditions (Amberlyst 15 catalyst, no solvent, 40°C, 4-6 hours), achieving the high producibility of dioxolanes with a yield higher than 90%.²⁶ The oxetane can be obtained from the catalytic upgrading of bio-derived monoterpenoids.³⁶

The results of this study help to identify how the chemical structure of renewable bioderived ethers influences both the sooting tendency and reactivity and serve as a foundational

Table 1. Tested fuels and their fuel properties

Fuel type	Chemical structure	Sooting tendency		Reactivity		LHV (MJ/kg)	Purity
		YSI	YSI/N _C	CN	CN/N _C		
Conventional diesel	N/A	111.4 – 246.0 ^{37,38}	8.0 – 17.6 ^b	40 – 51 _{CN} ^{39,40}	2.9 – 3.6 ^b	42.9 ⁸	N/A
Di- <i>n</i> -amyl ether (DAE)		49.8 ⁴¹ (5.0)	5.0 (0.5)	111.0 _{DCN} ⁴² (3.8 ⁴³)	11.1 (0.4)	39.0 ⁴⁴	>98%
4-butoxy-heptane (4BH)		60.3 ⁴¹ (5.0)	5.5 (0.5)	80.0 _{ICN} ⁸ (4.0)	7.3 (0.4)	40.0 ⁴⁴	>95%
3,3-dimethyl-oxetane (DMO)		27.8 ^c (5.0 ^c)	5.6 (1.0)	9.9 _{ICN} ^c (1.2 ^c)	2.0 (0.2)	36.5 ⁴⁵	98%
2-ethyl-4-methyl-1,3-dioxolane (EMD)		24.0 ^c (5.0 ^c)	4.0 (0.8)	17.5 _{ICN} ^c (0.4 ^c)	2.9 (0.1)	29.5 ^d	99%
2-isobutyl-4-methyl-1,3-dioxolane (IBMD)		45.2 ^c (5.0 ^c)	5.7 (0.6)	34.9 _{ICN} ^c (1.2 ^c)	4.3 (0.2)	32.3 ^d	>98%

^a Parenthesis: YSI measurement error/Reproducibility of CN measurements

^b Average N_C of typical diesel fuels assumed to be 14.

^c YSIs and ICNs measured in this study

^d Calculated using the G4 method

example for designing new biofuel candidates in advanced combustion devices.

Materials and Methods

Test fuel matrix

We describe the YSI and CN of the test fuels studied in comparison to conventional diesel in **Table 1**. Fuel properties are described with the values normalized to the number of carbon atoms, YSI/N_C, and CN/N_C, to isolate the structural effect from the effect of the number of carbon atoms. We chose five representative ethers to include various structural effects: Di-*n*-amyl ether (DAE) and 4-butoxy-heptane (4BH) as acyclic linear and branched ether, respectively. 3,3-dimethyl-oxetane (DMO) is a representative single-oxygen 4-membered cyclic ether. 2-ethyl-4-methyl-1,3-dioxolane (EMD) and 2-isobutyl-4-methyl-1,3-dioxolane (IBMD) are 5-membered cyclic ethers and contain two oxygens with a linear and branched alkyl group, respectively. The selected compounds contain a wide range of the main structural features of ether compounds (presence of a ring, primary to quaternary carbon types, number and position of oxygen atoms, etc.). This enables the test of structural features' effect on the fuel properties with the goal of supporting the future design of ethers. DAE, DMO, EMD, and IBMD were purchased from Sigma Aldrich or Fisher with a purity of at least 98%, and 4BH was obtained by synthesis at National Renewable Energy Laboratory (NREL) and had a purity of >95%.

Compared to conventional diesel,⁴⁶ these five compounds have lower YSI/N_C. The CN/N_C values of DAE, 4BH, and IBMD are higher than conventional diesel, manifesting their potential

applicability as a biodiesel blendstock. Although DMO and EMD have lower CN/N_C, they were also selected to investigate the structural effects of cyclic ethers on their YSI and CN. Of note, YSI/N_C and CN/N_C instead of YSI and CN were used here to compare and eliminate the difference stemming from carbon numbers. Ultimately, the carbon number effects are considered in our multivariate model, leading to the prediction of actual YSI and CN (*vide infra*).

It should be noted that the lower heating value (LHV) of fuel is one of the important fuel properties related to the energy density or maximum power of the powertrain. **Table 1** lists the LHV of five tested fuels from either the experimental or computational method (G4 composite). All of the tested fuels have a lower LHV than the conventional diesel owing to the presence of oxygen atom, spanning from 29.5 to 40.0 MJ/kg depending on the molecular structure. Given the disadvantageous impact of an oxygen atom on LHV, it is important to understand what is the best structure of ethers with the given chemical formula (given LHV) to maximize the benefit of the ether functional group to CN and YSI, which will be discussed further in the following sections.

The present study did not include one of the important classes of ethers: polyoxymethylene ethers (POMEs). The POMEs are known for their low sooting tendency, high reactivity, and the synthesizability of renewable resources.⁴⁷ There are many studies on its combustion characteristics,⁴⁸ and the detailed kinetics model is also available for some POMEs.⁴⁸ Meanwhile, the present study focused more on the molecular features whose role in the combustion chemistry has not been significantly exploited; branched structure, ring structure, and additional oxygen atom in a ring. Moreover, the important

ARTICLE

Sustainable Energy & Fuels

molecular features in POMEs are included in DAE, EMD, and IBMD; thus, we believe the CN and YSI of POME can be inferred based on the results of the present study.

YSI and CN measurement

The YSI and ICN (Indicated CN) values of DMO, EMD, and IBMD were measured in the present study using a co-flow diffusion flame burner at Yale University⁵⁰ and an Advanced Fuel Ignition Delay Analyzer (AFIDA) at NREL,⁵¹⁻⁵³ respectively. As the details of experimental procedures are well-defined from the previous study,⁵²⁻⁵⁵ here we provide only a brief description of YSI and CN measurement. As per YSI measurement, the CH₄/N₂/air diffusion flame is prepared with the co-flow burner flows. The CH₄/N₂ mixture (mole fraction ratio 42:58) flows out of the tube and reacts with air from the annular region around the tube. Meanwhile, the 2-dimensional image of soot concentration at the flame tip is measured using a color-ratio pyrometry. The YSI of fuel is derived from the relative increment of soot concentration with the 1000 ppm doping of the test sample, which is then scaled by comparing it to those of *n*-hexane and benzene, whose YSI are defined as 30 and 100, respectively. The ICN from AFIDA is derived from the ignition delay time of the spray combustion. The sample fuel is injected into the constant volume chamber preheated to 853 K and pressurized to 17.5 bar. The pressure trace is measured to detect the occurrence of autoignition; then, the ignition delay time is converted to ICN through a pre-defined correlation curve.⁵² The ICN measurement is repeated 12 times and averaged to the final report value.

This study includes measurements made as CN, DCN (Derived CN), or ICN in **Table 1** but calls all cetane number values as CN for subsequent correlation and analysis. ASTM D6890⁴³ and D8183⁵² describe the uncertainty bound of DCN and ICN concerning the CFR engine's CN. The 95 % confidence range of the difference between DCN and CN is ~ 6 %, while that of ICN and CN is 6.3 – 7.5 %. The given uncertainty bound is small enough to treat DCN, ICN, and CN as a lumped description, keeping enough resolution to represent the auto-ignition characteristic of five tested fuels.

Flow reactor experiments

The flow reactor and Gas Chromatography (GC) analytical setup have been described in detail previously.⁵⁶⁻⁵⁸ Briefly, a straight quartz tube, open to the atmosphere, is heated in a ceramic furnace. Fuel, helium, and oxygen are introduced at the inlet of the tube, and the effluent of the flow reactor is sampled directly to a dual GC system capable of measuring products in the C₁ to C₁₄ range. Fuel is introduced via a syringe pump, and gas flows are metered via mass flow controllers. Helium flow was varied to maintain a constant residence time throughout the temperature range investigated. GC1 contains a flame ionization detector (FID) equipped with a methanizer and mass spectrometer (MS) and measures the product distribution from C₄ to C₁₄. The species are identified qualitatively by a comparison of the mass spectrum with the National Institute of Standards and Technology (NIST) Mass Spectral Library. The

identified species are then quantitated for their concentration using *n*-heptane as the standard with the effective carbon number method.⁵⁹ GC2 utilizes three detectors, an FID, and two thermal conductivity detectors (TCDs), to measure the C₁ to C₄ products and CO/CO₂, respectively. Species are quantitated directly against known gas standards (Air Gas) where available.

Measurement uncertainties are assumed to be about 15% for GC1 due to the use of comparison to *n*-heptane in the methanizer/FID, and variations in the sample delivery (syringe pump) and sampling system. GC2 quantitates lower molecular weight species, which are easier to volatilize and have direct calibration standards, and its uncertainty is assumed to be 10%. All of the experimental data from the flow reactor is from a single measurement.

The concentration of all the product species was described as the carbon yield, which is defined as **Eq. (1)**; N_{C_i} is the carbon number of the i^{th} product and $[X_i]$ is the molar concentration of the i^{th} product. The carbon yield enables tracking how the carbon atoms in the parent molecules are distributed to the products, which is intuitively connected to the soot concentration. For example, a 1% mole fraction of C₇H₁₆ contributes to the soot emission more than C₅H₁₀, which can be inferred from its higher YSI value (YSI_{C₇H₁₆}=36.0 and YSI_{C₅H₁₀}=24.6). The higher YSI of C₇H₁₆ can be simply attributed to the higher carbon number in C₇H₁₆. However, counting each product based on the mole fraction cannot account for this difference in the potential contribution of each product species having a different carbon number. On the other hand, the carbon yield weighs the mole fraction based on the carbon number of the product species, so it is expected better to represent the soot characteristics of each ether fuel.

$$(\text{Carbon Yield})_i [\%] = \frac{N_{C_i}[X_i]}{\sum_i N_{C_i}[X_i]} * 100 \quad (1)$$

Computational details

The quantum-mechanical (QM) calculation was executed with Gaussian16 software.⁶⁰ Optimizations of all closed and open-shell reactants, products, and transition state (TS) structures were performed at the B3LYP/6-31G(2df,p) level of theory. Further optimization was then performed using the G4 composite method,⁶¹ which gives formation enthalpies of 38 open- and 45 closed-shell species with 1.1 and 1.5 kcal/mol confidence intervals, respectively, compared to experimental values.^{62, 63} The higher uncertainty for closed-shell species is presumably due to having problematic molecules in the dataset, such as oxirene and oxalic acid. However, the G4 method shows the accuracy compared to chemical accuracy (errors below 1.0 kcal/mol) for both open- and closed-shell species. Moreover, the dataset for benchmarking the G4 method contains various hydrocarbons, oxygenates, and their radicals that can be formed from the breakdown of ethers, further demonstrating the reliability of G4 in studying ethers. The validity of all TS was confirmed by identifying one imaginary frequency with a displacement vector connecting the correct reactant and product well geometries. Furthermore, intrinsic reaction coordinate (IRC) calculations at the B3LYP/6-

31G(2df,p) level of theory were performed to further confirm the nature of TSs.

All of the energetics in the following sections were based on the free energy rather than internal energy or enthalpy because it is directly related to the equilibrium/rate constant of reactions. To obtain free energies, thermochemistry calculation methods in Gaussian16 were used. Translational, electronic, rotational, and vibrational partition functions were calculated based on the statistical mechanics of ideal gas to quantify the contributions of each motion to internal energy, entropy, and free energy. Point group symmetry was considered when evaluating the rotational entropy of a molecule. Grimme's quasi-harmonic entropy correction was applied using GoodVibes⁶⁴ to remove vibrational entropy errors stemming from frequencies below 100 cm⁻¹.⁶⁵ The same package was also used in calculating free energies of optimized structures at the temperature relevant to YSI and CN:⁶⁴ 1500 K, and 700 K, respectively. 1500 K corresponds to the temperature at 30 mm above the co-flow diffusion flame burner of Yale University,⁵⁰ where the soot precursor concentration is maximized according to the numerical simulation of Xuan and Blanquart.⁶⁶ 700 K was selected as a representative temperature at the start of injection of CFR engine, which is the standard engine for CN measurement.⁶⁷ Considering the high-reactivity of ether compounds, the compression ratio of the CFR engine was assumed to correspond to the CN100 condition.

For each reaction pathway, free energies of intermediates, TSs, and products were obtained by setting the energy of the initial ether molecule to zero and calculating the difference relative to the reactant ether molecule. This enables the comparison of reaction kinetics of ethers with different stoichiometries based on the transition state theory.

Results and discussion

High-temperature combustion: YSI and soot precursor characteristics

To elucidate the structural effects on the sooting tendency of ethers, soot precursors were characterized from the flow reactor experiments at atmospheric pressure (82.1 kPa in Denver, USA), a residence time of 2.0 s, fuel-rich conditions ($\phi=3$), and 750–1100 K. **Figure 2A** presents the key results from flow reactor experiment of five test fuels, showing the carbon yield of fuel and hydrocarbon (HC) products; the detailed results including carbon yield of oxygenates, CO and CO₂ are available in **Section S1.1** of **ESI†**. The pie charts in **Fig. 2A** show the size distribution of HC products at 925 and 1100 K. This categorized presentation of product distribution is employed to simplify the analysis, as our focus was not on the detailed chemical kinetics of each ether fuel but on the size distribution of hydrocarbon products, which can become a soot precursor in the flame. For future reference, we also attached the raw data file from the flow reactor experiment to the **ESI†**.

All the tested fuels showed decreasing size of HC products as temperature increases. Interestingly, the size distribution at 1100 K has a noticeable correlation with YSI/ N_c of the fuel: the

higher portion of large HC products (C₃ & C₄), the higher YSI/ N_c values (the detailed discussion is included in the **ESI†**). In this regard, the following analysis will be focused on how the molecular structure of ethers is related to the size distribution of HC products and why the larger HC products lead to higher YSI/ N_c values.

Comparing the results from two acyclic ethers, DAE (YSI/ $N_c=5.0$) and 4BH (YSI/ $N_c=5.5$) (**Fig. 2A**), there are key observations relevant to their difference in YSI. That is, the 4BH shows (i) a lower onset temperature of fuel consumption and (ii) more C₃ species formation at 1100 K than DAE (19.3 % for 4BH vs. 14.6 % for DAE), both of which are likely to contribute to its higher YSI/ N_c than DAE. To justify that (ii) is related to the higher YSI, a detailed analysis was carried out on the soot formation pathway of C₂–C₄ HCs. The C₃ HC products from the flow reactor experiment mainly consist of propene, propyne, and allene, whereas ethylene and butene are major C₂ and C₄ species, respectively (**Section S8** in **ESI†**). We investigated the rate of elementary reactions relevant to the formation of benzene or fulvene from these HCs.^{68, 69} The benzene and fulvene can be formed from the recombination of propargyl (C₃H₃) or allyl radical (C₃H₅), which is readily produced through the hydrogen abstraction of HCs from allene and propene. The rate of such a recombination is $\sim 6 \times 10^{-12}$ cm³/molecules/s, which is two orders of magnitude faster than C₂ + C₄ recombination forming benzene.^{69, 70} Therefore, we presumed that the higher concentration of C₃ HCs likely contributes to more a soot precursor formation from 4BH than DAE.

A mechanistic study was carried out to explain these differences in between DAE and 4BH (**Fig. 2B**). It consists of three steps: (i) proposal of hypothetical reaction mechanisms for the formation of products observed from flow reactor experiments, (ii) QM energy calculations to validate the reasonableness of the hypothetical mechanism, and (iii) comparison of reaction energetics among five ethers to explain different product distributions. The main body of this paper only provides the explanation of the key reaction steps, and the full mechanisms are included in **Fig. S3** of **ESI†**.

DAE forms **DAE-I1** through hydrogen abstraction from the weakest C-H bond (see **Section S5** of **ESI†**) with the reaction free energy (ΔG) of -33.6 kcal/mol. Then, β -scission occurs (**DAE-I1**→**DAE-I2**) to yield pentanal and pentyl radical with an energy barrier (ΔG^\ddagger) of 22.8 kcal/mol. Next, pentanal in **DAE-I2** decomposes into C₂ species by releasing CO, followed by β -scission.⁷¹ Meanwhile, pentyl radical in **DAE-I2** is the major source of C₃ HCs from DAE oxidation; it forms C₁–C₃ species from through subsequent β -scission (pentyl → propyl + ethylene; propyl → propene + H; propyl → methyl + ethylene). Moreover, all general alkyl radicals, such as pentyl, can recombine with HO₂ and dissociate to the alkoxy + OH, followed by β -scission of alkoxy to aldehyde + H.^{72, 73} The hydrogen abstraction from the carbonyl side of the aldehyde leads to prompt disposal of CO, which can be a major source of CO formation from the alkyl radical. The pentyl radical can also release one hydrogen, leading to 1-pentene (**DAE-I3**), with a ΔG^\ddagger of 37.0 kcal/mol. The 1-pentene undergoes hydrogen abstraction and subsequent β -scission to produce C₂ and C₃ HCs.

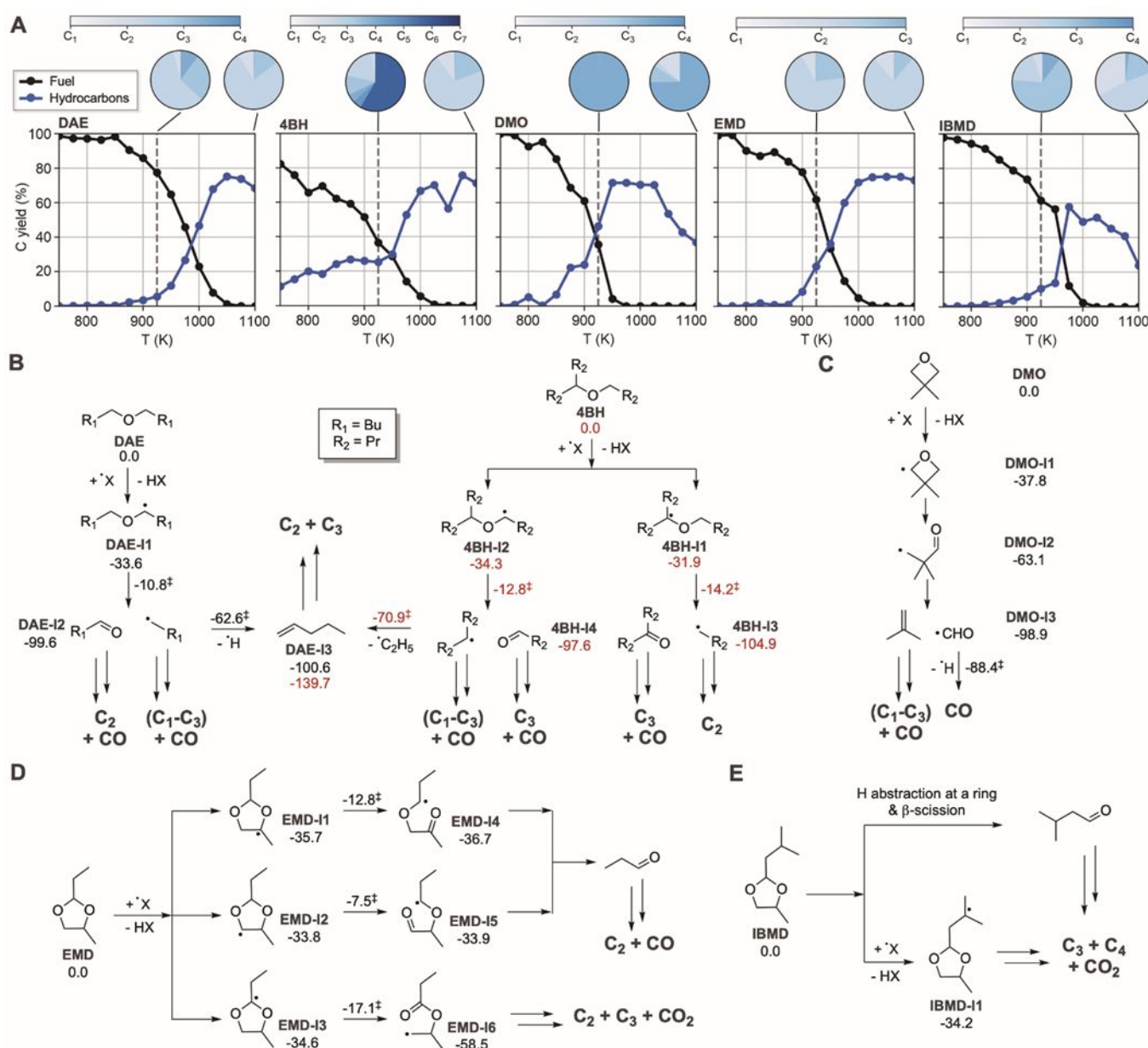


Figure 2. The results from (A) flow reactor experiments, and computational mechanistic studies at high-temperature combustion regime for (B) linear ethers (DAE and 4BH) and cyclic ethers (C) DMO, (D) EMD, and (E) IBMD. The pie chart shows the distribution of carbon numbers in HC products. For computational analysis, relative free energies were calculated at 1500 K using the G4 composite method (all units in kcal/mol). The energetics of all the hydrogen abstraction reaction assumes the OH radical as an H acceptor, as it is one of the most common and reactive radicals in the combustion environment, while any radical species also can be an H acceptor for hydrogen abstraction.

On the other hand, two hydrogen abstractions are possible for **4BH** with ΔG^\ddagger of -31.9 and -34.3 kcal/mol (**4BH-I1** and **4BH-I2**, respectively). Each radical intermediate then undergoes β -scissions with ΔG^\ddagger of 17.7 and 21.5 kcal/mol (**4BH-I1** \rightarrow **4BH-I3** and **4BH-I2** \rightarrow **4BH-I4**, respectively). These values are lower than that of DAE (22.8 kcal/mol), explaining the lower onset temperature of fuel consumption of 4BH (<750 K) than DAE (850 K) observed from the flow reactor experiment. Next, The 4-heptanone and butyl radicals in **4BH-I3** decompose into C₁–C₃ HCs and CO, as suggested in previous studies regarding the ignition of C₃–C₅ ketones.⁷⁴ Meanwhile, the butanal in **4BH-I4** oxidizes into CO and propyl radical (C₃).⁷¹ The heptyl radical in **4BH-I4** forms either C₇ (3-heptene) or C₅ (1-pentene) HCs

through the β -scission or the radical-radical hydrogen abstraction, latter of which has been recently recognized as an important class of reaction in the combustion by Wu et al.⁷⁵ Both 3-heptene and 1-pentene are further dissociated into C₁–C₃ HCs⁷⁶ via the hydrogen abstraction and subsequent β -scission. The heptyl radical, as pentyl radical does, can recombine with HO₂ and forms the butanal (3-heptoxy \rightarrow butanal + propyl), which disposes of the CO after the hydrogen abstraction from the carbonyl site. Of note, no aromatic compounds were observed until the temperature of 1100 K in flow reactor experiments, despite the presence of C₇ species (3-heptene and heptyl radical). This indicates the significance of C₃

HCs on aromatic soot precursor formation at a higher temperature around 1500 K.^{69, 70}

The mechanisms and product distribution discussed above provide clear evidence to support a higher YSI of 4BH than DAE. The higher YSI of 4BH is because it has more reaction channels producing C₃ HCs with a lower ΔG^\ddagger than DAE. The β -scission of the pentyl radical is only the major reaction channel for C₃ species formation from DAE, whereas four intermediates from 4BH (3-heptene, 4-heptanone, 1-pentene, and butanal) can produce C₃ HCs.^{71, 74, 76} This is consistent with a slightly higher portion of C₃ HC from 4BH than DAE observed from the flow reactor experiment at 1100 K.

To compare acyclic and cyclic ethers, structural effects of DMO (YSI/N_C=5.6) on its YSI were investigated using flow reactor experiments (Fig. 2A). The fuel consumption gives rise to acyclic C₄ HCs. Interestingly, the concentration of C₄ HCs is still high at 1100 K, whereas the C₅ and C₇ HCs from DAE and 4BH all decompose at the same temperature. The oxidation of DMO is initiated by hydrogen abstraction followed by a ring-opening reaction (DMO→DMO-I1→DMO-I2, Fig. 2C), as confirmed by the jet-stirred reactor experiment of Dagaut et al. on the simplest oxetane.⁷⁷ Then, DMO-I2 generates *iso*-butene and formyl radical (DMO-I3), and they are readily oxidized into CO and smaller HCs (Detailed mechanisms in Fig. S3(c) of ESI†). The 2-methyl allyl radical formed from *iso*-butene has high stability owing to the resonance stabilization, leading to more C₄ HCs at 1100 K. Additionally, the 2-methyl allyl dissociates to allene and can be a dominant source of propargyl radical (C₃H₃) through subsequent hydrogen abstraction, which is one of the strongest soot precursors⁶⁸ leading to high YSI. Therefore, the higher YSI/N_C value of DMO than DAE is attributed to the *iso*-C₄ HCs originating from the quaternary carbon and their decomposition to propargyl radical. It is noteworthy that the YSI/N_C of 4BH and DMO are comparable (5.5 vs. 5.6, respectively) despite higher C₄ yields from DMO than 4BH. This is consistent with the higher effectiveness of C₃ species for aromatic formation relative to C₄ species, which is also in line with higher sooting tendency of propyne than *iso*-butene.⁷⁸

Our investigation was expanded to dioxolanes, as shown in Figs. 2D and 2E. Similar to DMO, the fuel consumption of EMD (YSI/N_C=4.0) raises the concentration of acyclic C₂–C₃ HCs. The HCs at 1100 K consist of C₁–C₃, contrary to abundant C₄ HC from DMO. The ring-opening is driven by hydrogen abstractions at the C–H bonds located at the carbon adjacent to oxygen atoms,²⁹ forming EMD-I1, EMD-I2, and EMD-I3. Their rings are then opened by breaking a C–O bond, resulting in EMD-I4, EMD-I5 and EMD-I6. They are eventually decomposed into HCs (ethylene, propene) and propanal. Propanal can be converted into C₂ HCs by releasing CO, explaining that the major HC is C₂ at 1100 K (Full mechanisms are shown in Fig. S3(d) of ESI†). In other words, soot precursor from EMD oxidation mainly consists of small C₂ species owing to the location of oxygen atoms in the ring, leading to propanol that decarbonylates giving ethylene, which contribute to the lower YSI/N_C of EMD than DAE, 4BH, and DMO that showed more C₃ or C₄ HC formation.

To elucidate the effect of branched alkyl groups in cyclic ethers, distributions of soot precursors and their pathways were investigated for IBMD (YSI/N_C=5.7) and compared with EMD. From the flow reactor experiments, IBMD showed a different distribution of HCs compared with those from EMD; more C₃ and C₄ HCs were observed from IBMD than from EMD (19.4 % for IBMD and 11.0% for EMD). Overall reaction pathways of IBMD derived from experiments are analogous to EMD (hydrogen abstraction at the ring carbon followed by ring-opening and β -scissions). However, the major oxygenates and HCs are different owing to the presence of the tertiary carbon in the substituted *iso*-butyl group that undergoes hydrogen abstraction to form IBMD-I1. The hydrogen abstraction at a ring followed by β -scission mainly produces 3-methylbutanal, whereas IBMD-I1 subsequently decomposes into propene and *iso*-butene (Fig. 2E, detailed mechanisms in Fig. S3(e) of ESI†). In other words, the branched structure in IBMD leads to higher yields of larger HCs (C₃–C₄) than EMD, and these HCs engage in more aromatic soot precursor formation^{69, 70, 79} than C₁ and C₂ as discussed above. This explains the higher YSI value of IBMD than EMD (YSI/N_C=4.0).

In summary, different structural features of acyclic and cyclic ethers affect the size distribution of the HC products formed. Particularly, tertiary and quaternary carbons in ethers lead to a higher portion of C₃ or C₄ HCs relative to C₂, thereby, yielding increased formation of aromatic soot precursors, while the location of oxygen atoms are key to reducing the size of HC products. These results provide further mechanistic insights into the structural effects on sooting tendencies of ethers and motivate the design of low-sooting ethers through a multivariate analysis (*vide infra*).

Low-temperature combustion: cetane number and reactivity

CN is the fuel property indicating the autoignition delay at compression ignition (CI) engine-relevant conditions. Due to high pressure (10–40 bar) and moderate temperature (700–900 K) in the cylinder over the duration of fuel injection, the combustion chemistry determining CN is distinct from that determining YSI, and is referred to as low-temperature chemistry. Low-temperature chemistry is initiated by the reaction between O₂ and fuel radicals forming peroxide radical RO₂ and isomerization of RO₂ to hydroperoxide radicals, QOOH. It is then followed by chain propagation reactions such as the second O₂ addition making O₂QOOH and its isomerization into keto-hydroperoxide (KHP) + OH. Because of the comparable time scale of low-temperature reactions to the combustion in CI engines (~a few milliseconds), the energy barriers of low-temperature reactions affects the dynamics of the combustion process in CI engines such as combustion phasing, heat release rate, or cyclic variation. For example, a fuel with low CN (long ignition delay) allows a longer mixing time for fuel and air in the CI engine. The increased homogeneity of fuel-air mixture sometimes leads to the abrupt heat release rate of the combustion phase,⁸⁰ preventing high-load operation of CI engines due to the noise, vibration, and endurance issues.

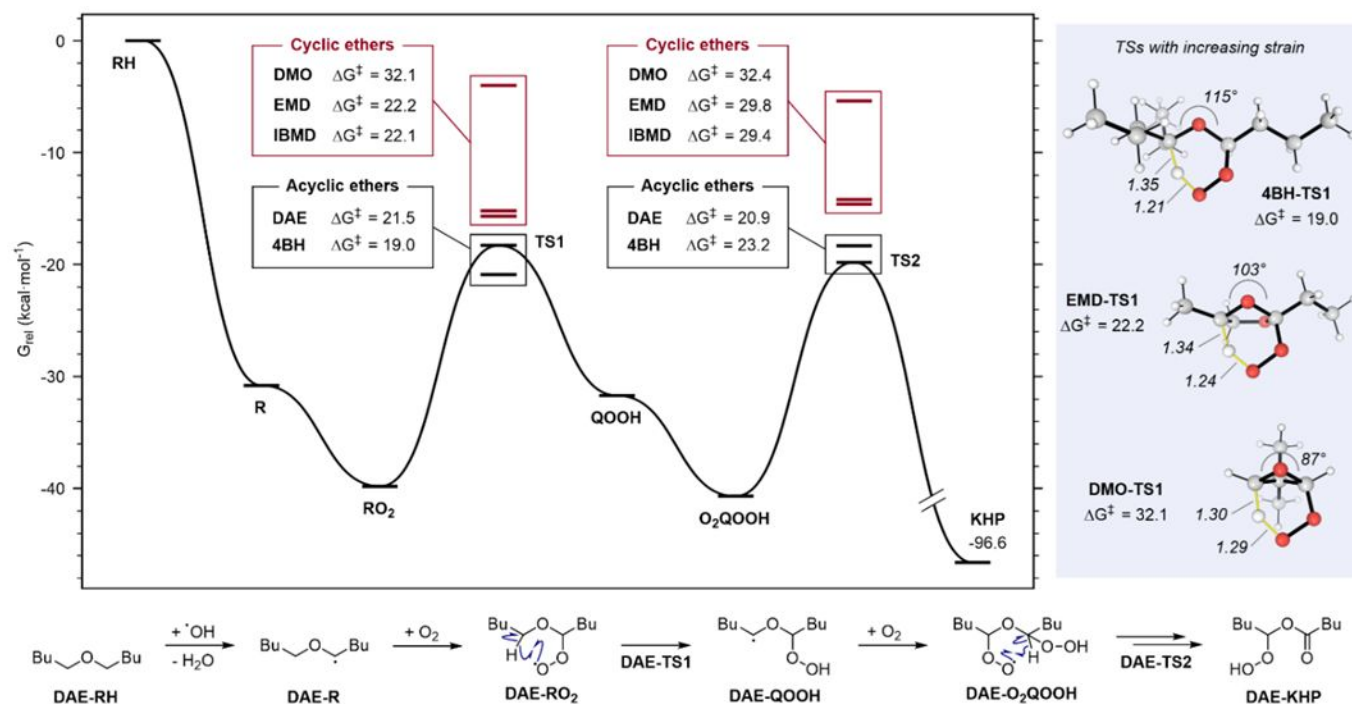


Figure 3. Relative Gibbs free energy profile (G_{rel} in kcal/mol) for DAE decomposition at low-temperature combustion regime. The barriers heights (ΔG^\ddagger) of $RO_2 \leftrightarrow QOOH$ relative to RO_2 (and those of $O_2QOOH \leftrightarrow KHP + OH$ relative to O_2QOOH) were calculated for all the ethers tested. Representations of TS1 for ethers with different structural properties are shown on the right side. Bonds included in the TSs are represented as thin yellow lines with distances in Å. All the energetics was calculated at 700 K.

Low-temperature reactivity is essentially the rate of low-temperature reaction steps. Thus, CN is proportional to the rate (thus, anti-proportional to the energy barrier) of consecutive reactions from hydrogen abstraction to KHP formation. In this regard, we calculated the energetics along the low-temperature reaction pathway of five tested fuels and analyzed how the energy barriers depend on the fuel structure. It should be noted that only hydrogen abstraction reactions from weak C-H bond were considered initial reactions. C-H bond dissociation energies were estimated with ALFABET,⁸¹ a graph neural network model of bond dissociation energy. Further details on predicted C-H bond energetics are discussed in Section S5 of ESI†. Next, we assumed that the hydrogen migration reactions ($RO_2 \leftrightarrow QOOH$ and $O_2QOOH \leftrightarrow KHP + OH$) dominantly occur between these weak C-H bonds through a 6-membered transition state (TS), which can be inferred by the rate rules of Villano et al.⁸²

Figure 3 shows the potential energy surface diagram of DAE in a low-temperature chemistry regime with highlights on the difference in the energy barrier of $RO_2 \leftrightarrow QOOH$ and $O_2QOOH \leftrightarrow KHP + OH$ for five tested fuels (the detailed energetics are in Section S2 of ESI†). As expected from the higher CN values of acyclic ethers relative to cyclic ethers, DAE and 4BH show lower energy barriers than DMO/EMD/IBMD in TS1 (19.0 – 21.5 vs. 22.1 – 32.1 kcal/mol) and TS2 (20.9 – 23.2 vs. 29.4 – 32.4 kcal/mol). The differences in reactivity most likely arise from the structural strain arising from the six-membered TSs. In acyclic ethers, the system can accommodate six-membered cyclic TSs with little distortion from the expected angle of this type of ring structure (115° for 4BH vs. approximately 110° for typical six-membered aliphatic rings). Contrarily, the angle strain for cyclic

ethers is much higher since the C-O-C substructure cannot adapt as freely as in the previous case (103° and 87° for EMD and DMO, respectively). This ability of the systems to reduce angle strain causes major differences in the energy profiles of acyclic and cyclic ethers, with energy barriers that can differ by as much as 13.1 kcal/mol (TS1 of 4BH vs. DMO). A complete analysis of the ΔG^\ddagger with varying types of carbon (from primary to quaternary) is presented in Section S3 of ESI†.

To support the QM calculation, flow reactor experiments were executed at atmospheric pressure, a residence time of 2.0 s, an equivalence ratio of 1, and a temperature range of 400 – 700 K. Fig. 4A depicts the carbon yield of fuel and intermediates related to low-temperature chemistry (LTI; low-temperature intermediates) from flow reactor analysis. The LTI consist of product species containing more than two oxygen atoms since low-temperature chemistry consists of consecutive O_2 addition at the radical site, producing products with high oxygen content. Additionally, the cyclic products from acyclic parent fuels were also considered as LTI as well because cyclization is one of the chain propagating reactions in low-temperature chemistry.⁸³

DAE and 4BH showed negative temperature coefficient (NTC) behavior of fuel consumption and LTI production, consistent with their high CN. 4BH had a single NTC region at 450 K, while DAE showed two NTC regions at 500 and 625 K, respectively. The double NTC behavior was also observed for di-n-butyl ether in the jet-stirred reactor/flow reactor experiment of Tran et al.¹⁹ Similarly, the multi-stage ignition, which can be related to the multiple NTC behavior, has been detected from the rapid compression machine experiments on the di-n-butyl ether from Hakimov et al.⁸⁴ and the di-ethyl ether from Issayev

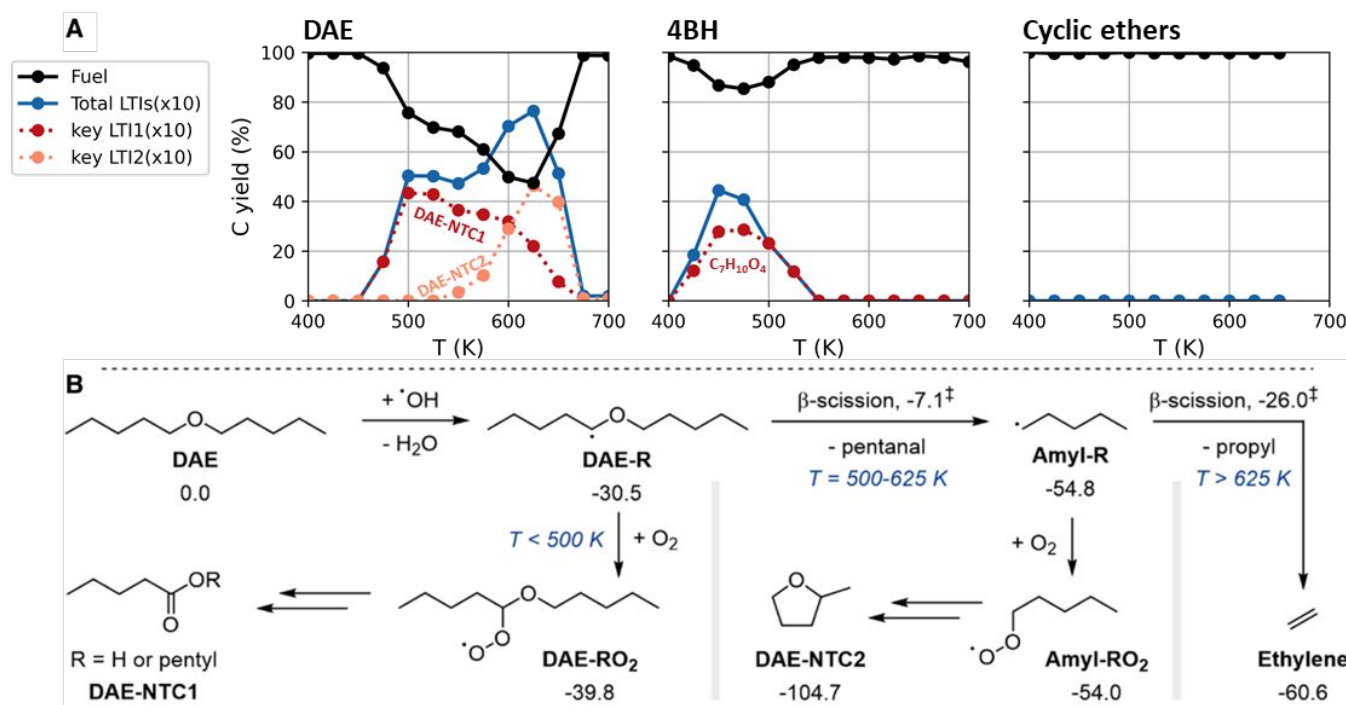


Figure 4. (A) Carbon yield of fuel (black), total LTIs (blue), key LTIs (red and orange dotted lines) from flow reactor experiments of DAE, 4BH, DMO, EMD, and IBMD at 400 – 700 K, $\phi = 1$, at atmospheric pressure and residence time of 2.0 s, corresponding to the low-temperature combustion regime. (B) Reaction pathway related to the double NTC behavior of DAE with energies calculated at 700 K using G4 and presented in kcal/mol.

et al.⁸⁵ QM calculations pertinent to the double NTC behavior of DAE were conducted and summarized in Fig. 4B. The fuel consumption and LTI production at the 2nd NTC of DAE are much higher than those of the 1st NTC, so one would expect it to be related to higher CN of DAE than 4BH. In this regard, we show the molecular structure of the major LTI at each NTC region to elucidate the mechanism of the double-NTC behavior of DAE. At the 1st NTC region the LTI consist mainly of pentanoic acid and pentyl pentanoate (DAE-NTC1) - the former is from hydrogen migration of QOOH forming the aldehyde and OH radical,⁸⁶ and the latter is from Korcek's mechanism for KHP decomposition.⁸⁷ The concentration of 2-methyl tetrahydrofuran (DAE-NTC2) rapidly increases at 500 – 625 K and makes up the majority of LTIs (60.7 %) at the 2nd NTC (625 K). Of note, the majority of LTI from 4BH oxidation was C₇H₁₀O₄, whose molecular structure was not identified from mass spectroscopy.

At the temperature of <500 K, the fuel radical from DAE (DAE-R) is likely to react with O₂ and go through low-temperature chemistry, as described in Fig. 3. Above 500 K, the 23.4 kcal/mol ΔG^\ddagger of the β -scission from DAE-R is overcome (DAE-R \rightarrow Amyl-R). The channel switches from DAE-R \rightarrow DAE-RO₂ to DAE-R \rightarrow Amyl-R reduces the overall reactivity since the former pathway produces OH radicals while the latter does not, which should be observed as the 1st NTC behavior in the flow reactor experiment. The subsequent β -scission of pentyl radical (Amyl-R \rightarrow Ethylene) has a higher energy barrier of 28.8 kcal/mol and as a result, the pentyl radical (Amyl-R) is likely to react with O₂ and proceed with its own low-temperature chemistry pathway, producing 2-methyl tetrahydrofuran + OH radical (DAE-NTC2) through cyclization reaction of QOOH. As the temperature goes above 625 K, the ΔG^\ddagger of β -scission from

pentyl radical can be overcome as well, and the channel switching between Amyl-R \rightarrow Amyl-RO₂ to Amyl-R \rightarrow Ethylene occurs. This channel switching contributes to lower the overall reactivity (2nd NTC) again because it deactivates the 2-methyl tetrahydrofuran formation reactions, which is a source of reactive OH radicals. Therefore, the presence of 2nd NTC behavior is attributed to the chain propagation reaction (Amyl-R \rightarrow Amyl-RO₂ \rightarrow DAE-NTC2) available even after the chemistry of DAE switches to high-temperature chemistry (DAE-R \rightarrow Amyl-R). It is owing to the high energy barrier of pentyl radical dissociation (Amyl-R \rightarrow Ethylene), which must contribute to further enhancing the reactivity of DAE compared to 4BH. It is noteworthy that the high reactivity of 4BH observed in Fig. 2A should not be correlated to its CN. The flow reactor experiment in Fig. 2A is dictated by high-temperature chemistry in the absence of LTI production, whereas CN is related to the low-temperature chemistry involving LTIs as shown in Fig. 4.

In comparing the cyclic ethers, there are two major differences; 1) ring size and 2) the number of oxygen atoms. First, the size of the ring was investigated using a systematic calculation of RO₂ \leftrightarrow QOOH with varying ring sizes (4-membered, 5-membered, or 6-membered ring), and the results are included in Section S3 of ESI[†]. The energy barrier of RO₂ \leftrightarrow QOOH was found to be remarkably sensitive to ring strain. The highest energy barrier, thus the lowest reactivity, was observed from the case where both carbons participating in RO₂ \leftrightarrow QOOH are in a 4-membered ring with the highest ring strain. This explains the large energy barrier calculated for TS1 of DMO (32.1 kcal/mol, Fig. 3). Meanwhile, the energy barrier decreased as the ring size increased. The results presented in Fig. 3 for DMO, EMD, and IBMD agree with the systematic study; the ΔG^\ddagger

ARTICLE

for **TS1** for EMD and IBMD are on average ~ 10 kcal/mol lower than those of DMO. This is attributed to the difference in ring strain between 4- and 5-membered rings.

The impact of additional oxygen atoms was isolated by comparing the overall energetics of low-temperature chemistry from EMD and 2-ethyl-5-methyl-tetrahydrofuran (EMTHF), which has one less oxygen atom than EMD, and its results were summarized in **Section S4** of **ESI†**. Comparing the energy barriers of each reaction step it is obvious that the kinetic effect of the oxygen atom is only around ~ -3 kcal/mol, which is comparably smaller than the other structural effects such as branching or cyclization. However, it was found that the thermodynamics to KHP is significantly favored for the case of EMD. Therefore, the second oxygen in the ring greatly stabilizes (up to 19.7 kcal/mol lower) the reactive intermediates throughout the low-temperature chemistry and facilitates the formation of LTI.

Meanwhile, the higher reactivity of IBMD than EMD is an interesting feature, considering that the branched structure in acyclic ethers generally reduces the reactivity, as we have seen in DAE vs. 4BH. One of the key differences between EMD and IBMD is the presence of a tertiary carbon. This tertiary carbon in IBMD enhances the rate of hydrogen abstraction reaction with its low C-H bond dissociation energy. The different dependency of low-temperature chemistry on the branched structure in cyclic and acyclic structure will be key to better understanding CN's structure-property relationship.

Additionally, it should be noted that the low-temperature chemistry of cyclic ethers may compete with the ring-opening reaction, as Fenard et al. show through the detailed kinetics study on the tetrahydrofurans (THF).⁸⁸ The present study did not exploit this competition further owing to the absence of evidence for a low-temperature reaction from cyclic ethers in **Fig. 4**; the energetics relevant to the ring-opening reaction was included in **Fig. 2** as part of high temperature combustion, though.

Guide for the future design of diesel fuels with improved sooting tendency and cetane number

The insights gained from the five ethers can be generalizable to a broader scope of ethers for the rational design of bioderived ethers with low YSI and high CN. First, YSI and CN of 50 ethers, at least one of whose CN or YSI values have been studied experimentally, were curated in **Section S6** of **ESI†**. The missing CN or YSI of some species were predicted using in-house machine-learning (ML) prediction models for YSI⁵⁴ and CN,³⁷ which were trained to 620 CN and 663 YSI database for single compounds with mean absolute error (MAE) of 5.7 and 4.9, respectively. Next, we devised the models accounting for the quantitative relationship between the molecular structure and YSI/CN values. Such models are necessary since it is labor-intensive to repeat all the above experimental and computational analyses for 50 ethers. Two simple linear regression models (LRMs) were developed for YSI and CN, as described in **Eq. (2)** and **Eq. (3)**:

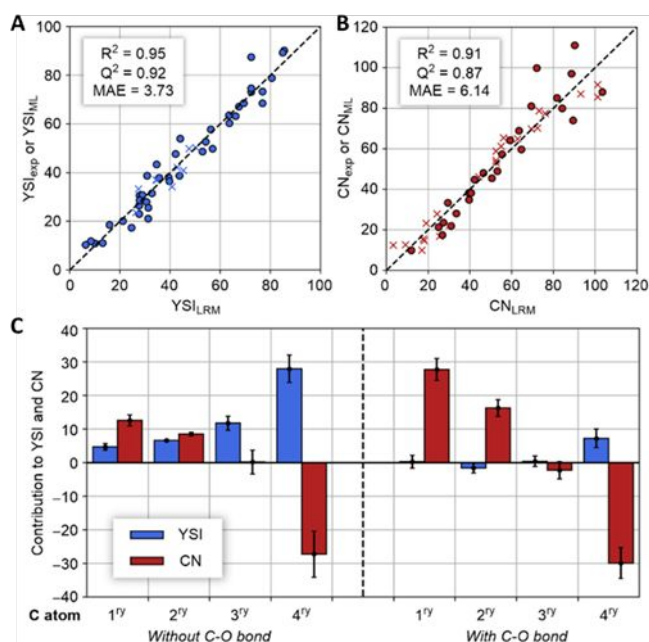


Figure 5. Reliability of linear regression models for (A) YSI and (B) CN. The dot and cross symbols denote the Y values from experiments (YSI_{exp} or CN_{exp}) and the in-house machine learning model (YSI_{ML} or CN_{ML}), respectively. The deterministic coefficients were evaluated with two different ways: 1) by treating the entire 50 ethers dataset as a training set (R^2) and 2) by the leave-one-out cross validation (Q^2). The fitting parameters representing the contribution of each carbon type to YSI or CN are compared in (C).

$$YSI_{LRM} = \alpha_0 + \sum_{i=1}^8 \alpha_i N_i \quad (2)$$

$$CN_{LRM} = \beta_0 + \sum_{i=1}^8 \beta_i N_i \quad (3)$$

The two models share the same eight structural features: the number of primary, secondary, tertiary, and quaternary carbon with/without C-O bond attached, respectively (N_i ; $1 \leq i \leq 8$). Of note, utilizing this set of descriptors enables the analysis of chemical structural effects on YSI and CN on a unified basis (details are discussed below). Moreover, all the N_i 's are simply obtained from 2D molecular structures, demanding no expensive QM calculations for generating molecular features. This is one of the key strengths of our model compared to others that require computational costs for generating the key descriptors, although it is only specialized for ethers. The nine coefficients for LRMs of YSI and CN – α_i and β_i , respectively – were then determined by the regression using the 50 ethers. The reliability of the LRMs for YSI and CN is depicted in **Fig. 5A** and **5B**. Each model reproduces the experimental and ML-derived YSI and CN values with an R^2 of 0.95 and 0.91, respectively. The MAE, RMSE, and max deviation were 6.14, 8.09, 27.78 for the CN regression model, 3.73, 4.82, and 15.18 for the YSI model. The overfitting possibility was attested with leave-one-out cross-validation, as shown in the Q^2 values of 0.92 and 0.87, implying the robustness of the derived model to the dataset.

It should be emphasized that each of the eight carbon types has different structural influences on YSI and CN, which can be

compared by analyzing the coefficients α_i and β_i (Fig. 5C; each α_i and β_i values are summarized in Section S7 of ESI†). α_i 's showed a clear dependency of YSI on the extent of branching of the carbons without C-O bonds; it increases in the order of primary<secondary<tertiary<quaternary. In other words, highly branched carbons contribute more to increasing YSI and thus are not favorable for designing low-emission fuels³⁰. This is consistent with the findings discussed in previous sections; the carbons in the branched structure are the source of C₃ and C₄ HC products, eventually leading to high soot concentration. On the contrary, the carbons with C-O bonds barely contribute to the sooting tendency, as can be seen from their small corresponding α_i 's. The carbons adjacent to oxygen atoms are eventually converted to carbon monoxide, so they are rarely involved in the soot precursor formation.

Meanwhile, β_i shows that the primary carbon contributes the most to enhance the CN, and its impact decreases in the order of primary>secondary>tertiary>quaternary, with the negative contribution of quaternary carbon. It can be inferred that the reactivity of fuel in the low-temperature regime decreases as the molecular structure gets branched with a fixed N_c. The same trends were shown regardless of the existence of adjacent oxygen atoms. However, the primary and secondary carbons attached to oxygen atoms are more effective in enhancing the reactivity of fuel than those without oxygens. The insights gained from β_i are in line with what we found in previous sections. First, the ethers with more branches showed less CN because branched ethers inhibit hydrogen migration reactions. Second, the oxygen atoms make the low-temperature reaction thermodynamically favorable and promote OH radical production.

The quantitative understanding from Fig. 5C gives us a useful guideline for designing ethers with low-soot formation and high-reactivity. In other words, one can build new ethers by tuning the number of carbons with specific types to minimize YSI and maximize CN and assemble carbon building blocks into one ether molecule. It is related with our "Fuel property first" principle for the screening and development of next generation biofuels before we synthesize many biofuel candidates in the lab.⁸⁹ More specifically, it is beneficial to have more carbon atoms corresponding to low α_i 's to design ethers with low emissions. In contrast, those with high-reactivity will maximize N_i 's associated with high β_i 's. For example, to achieve low YSI and high CN, one can maximize the number of primary or secondary carbons attached to the oxygen atoms, corresponding to the carbons with low α_i and high β_i . Therefore, polyoxymethylene dimethyl ether and 1,3,5-trioxane satisfy these conditions and can be promising candidates.

To verify the above hypothesis, we measured the YSI and CN of trioxane; it has a YSI/N_c of 1.1 (YSI=3.5) and a CN/N_c of 9.0 (CN=26.9 from the blending method that has uncertainty⁴²) while the conventional diesel is 17.6 and 3.1 of YSI/N_c and CN/N_c, respectively, in Table 1. The low YSI/N_c of trioxane results from the rapid decomposition into low-sooting formaldehyde.⁹⁰ Our computational results also show that formaldehyde formation from trioxane is kinetically and thermodynamically favorable ($\Delta G^\ddagger=35.0$ and $\Delta G=-95.6$

kcal/mol, at 1500 K). The lower YSI/N_c and higher CN/N_c of trioxane relative to other cyclic ethers and conventional diesel in Table 1 suggest that trioxane is potentially a desirable as a fuel molecule. It should be noted that the 1, 3, 5-trioxane is in a solid phase at room temperature, which is unsuitable for a typical IC engine application. So 1, 3, 5-trioxane should be considered a promising "building block" rather than using it. The melting point can be decreased by substituting the alkyl groups to make it a suitable fuel candidate. For example, paraldehyde, one of the simplest substituted trioxane, is a liquid at room temperature. Similarly, the CN of 1,3,5-trioxane also can be further improved by adding alkyl substitution, especially with many primary and secondary carbons.

In contrast, spark-ignition (SI) engine or advanced CI engines such as premixed-charge compression ignition (PCCI) engine and reactivity-controlled compression ignition (RCCI) engine are known to require low-reactivity fuel to improve the engine performance.^{34, 91} The quaternary carbon is the most effective building block for designing the low-reactivity fuel, but it has a detrimental impact on YSI. The high soot precursor formation from quaternary carbon can be moderated by placing oxygen atoms next to the quaternary carbon, as can be inferred from our QM analysis and Fig. 5C. As an example of low-emission and low-reactivity fuel candidates, we additionally carried out the experiments for 2,2-dimethyl-1,3-dioxolane (DMD), which has a quaternary carbon located between two oxygen atoms while its ring structure helps to further reduce the reactivity, as we discussed in Section S4 of ESI. The DMD has a modest YSI/N_c of 3.5 (YSI=17.4) and a low CN/N_c of 2.3 (CN=11.5), which are in the acceptable range for SI engine application (CN and YSI of iso-octane are 17 and 62, respectively). Moreover, The boiling point and density of DMD are 93 °C and 926 kg/m³, while those of iso-octane are 99 °C and 690 kg/m³. Most physical and chemical properties indicate the DMD is a promising candidate for low-reactivity fuel; further investigation is required on the other physical properties to ensure its feasibility.

Conclusions

This study examined how ethers' chemical structure affects sooting tendency and reactivity through flow reactor experiments and computational mechanistic studies for five representative ether molecules at two temperature regimes. From the high-temperature regime (700-1100K), it was revealed that the sooting tendency of ethers, quantified as the YSI, is related to the size distribution of HCs formed from their decomposition. The size of hydrocarbon soot precursors is controlled by the extent of branching, presence of a ring, and position and the number of oxygens. In particular, the existence of tertiary and quaternary carbons prevents further oxidation of HCs into smaller species. The structural effects on the reactivity of ethers, quantified as CN, were also investigated in the low-temperature regime (400-700K). It was found that the reactivity of fuel is related to the activation energies of RO₂↔QOOH and KHP formation reactions. Ring strain and the location of oxygen atoms are important features affecting the activation energy. Moreover, we found that the double NTC behavior of linear

ethers contributes to further improving their reactivity. Based on the insights gained from the above studies, structure-property relationships for YSI and CN were derived using a multivariate model. The model indicates that structures containing primary and secondary carbon atoms adjacent to the oxygen atom are promising building blocks for a low-sooting tendency and high-reactivity ethers.

Author Contributions

S.K. designed the research; J.C., Y.K., B.D.E., G.M.F., N.N., J.Z., Z.X., C.H., J.V.A.R., P.C.S., performed the research; J.C., Y.K., B.D.E., J.V.A.R., S.K. analyzed data; J.C., Y.K., B.D.E., G.M.F., N.N., J.V.A.R., P.C.S., B.T.Z., C.S.M., L.D.P., R.L.M., S.K. wrote the paper.

Conflicts of interest

There are no conflicts to declare.

Acknowledgements

This research was conducted as part of the Co-Optimization of Fuels & Engines (Co-Optima) project sponsored by the U.S. Department of Energy's Office of Energy Efficiency and Renewable Energy Bioenergy Technologies Office and Vehicle Technologies Office. Co-Optima is a collaborative project of several national laboratories initiated to simultaneously accelerate the introduction of affordable, scalable, and sustainable biofuels and high-efficiency, low-emission vehicle engines. Work at the National Renewable Energy Laboratory was performed under Contract No. DE347AC36-99GO10337. The work at Yale was based upon subcontract DE-A36-08GO28308 from the Alliance for Sustainable Energy, LLC, Managing and Operating Contractor for the National Renewable Energy Laboratory for DOE. A portion of this research was performed using computational resources sponsored by the Department of Energy's Office of Energy Efficiency and Renewable Energy and located at the National Renewable Energy Laboratory. The views expressed in the article do not necessarily represent the views of the DOE or the U.S. Government. The U.S. Government retains and the publisher, by accepting the article for publication, acknowledges that the U.S. Government retains a nonexclusive, paid-up, irrevocable, worldwide license to publish or reproduce the published form of this work, or allow others to do so, for U.S. Government purposes. Computer time was provided by the NSF Extreme Science and Engineering Discovery Environment (XSEDE), Grant no. TG-CHE210034 and by the National Renewable Energy Laboratory Computational Science Center.

References

1. D. Hountalas, G. Mavropoulos and K. Binder, *Energy*, 2008, **33**, 272-283.
2. S. Kook, C. Bae, P. C. Miles, D. Choi, M. Bergin and R. D. Reitz, *SAE transact.*, 2006, 111-132.
3. M. M. Pandian and K. Anand, *Appl. Therm. Eng.*, 2018, **142**, 380-390.
4. J. Gieshoff, A. Schäfer-Sindlinger, P. Spurk, J. Van Den Tillaart and G. Garr, *SAE Tech. Pap.*, 2000.
5. A. Datta and B. K. Mandal, *Renew. Sust. Energ. Rev.*, 2016, **57**, 799-821.
6. L. Cai, F. vom Lehn and H. Pitsch, *Energy Fuels*, 2021, **35**, 1890-1917.
7. L. Ou, S. Li, L. Tao, S. Phillips, T. Hawkins, A. Singh, L. Snowden-Swan and H. Cai, *ACS Sustain. Chem. Eng.*, 2022, **10**, 382-393.
8. N. A. Huq, X. Huo, G. R. Hafenstine, S. M. Tiffet, J. Stunkel, E. D. Christensen, G. M. Fioroni, L. Fouts, R. L. McCormick and P. A. Cherry, *Proc. Natl. Acad. Sci.*, 2019, **116**, 26421-26430.
9. N. M. Eagan, B. M. Moore, D. J. McClelland, A. M. Wittrig, E. Canales, M. P. Lanci and G. W. Huber, *Green Chem.*, 2019, **21**, 3300-3318.
10. D. J. Gaspar, C. J. Mueller, R. L. McCormick, J. Martin, S. Som, G. M. Magnotti, J. Burton, D. Vardon, V. Dagle and T. L. Alleman, *Top 13 Blendstocks Derived from Biomass for Mixing-Controlled Compression-Ignition (Diesel) Engines: Bioblendstocks with Potential for Decreased Emissions and Improved Operability*, Pacific Northwest National Lab.(PNNL), Richland, WA (United States), 2021.
11. P. Mohanan, N. Kapilan and R. Reddy, *SAE Tech. Pap.*, 2003, **2003-01-0760**.
12. Y. Zhou, N. Pavlenko, D. Rutherford, L. Osipova and B. Comer, *The potential of liquid biofuels in reducing ship emissions*, International Council on Clean Transportation, 2020.
13. K. Yasunaga, F. Gillespie, J. Simmie, H. J. Curran, Y. Kuraguchi, H. Hoshikawa, M. Yamane and Y. Hidaka, *J. Phys. Chem. A*, 2010, **114**, 9098-9109.
14. Y. Sakai, J. Herzler, M. Werler, C. Schulz and M. Fikri, *Proc. Combust. Inst.*, 2017, **36**, 195-202.
15. M. Werler, L. R. Cancino, R. Schießl, U. Maas, C. Schulz and M. Fikri, *Proc. Combust. Inst.*, 2015, **35**, 259-266.
16. A. D. Danilack, S. J. Klippenstein, Y. Georgievskii and C. F. Goldsmith, *Proc. Combust. Inst.*, 2020, **38**, 671-679.
17. N. Belhadj, R. Benoit, P. Dagaut, M. Lailliau, Z. Serinyel and G. Dayma, *Proc. Combust. Inst.*, 2021, **38**, 337-344.
18. S. Thion, C. Togbé, Z. Serinyel, G. Dayma and P. Dagaut, *Combust. Flame*, 2017, **185**, 4-15.
19. L.-S. Tran, J. Wullenkord, Y. Li, O. Herbinet, M. Zeng, F. Qi, K. Kohse-Höinghaus and F. Battin-Leclerc, *Combust. Flame*, 2019, **210**, 9-24.
20. Z. Serinyel, G. Dayma, V. Glasziou, M. Lailliau and P. Dagaut, *Proc. Combust. Inst.*, 2021, **38**, 329-336.
21. C. R. Mulvihill, A. D. Danilack, C. F. Goldsmith, M. Demireva, L. Sheps, Y. Georgievskii, S. N. Elliott and S. J. Klippenstein, *Energy Fuels*, 2021, **35**, 17890-17908.
22. H. J. Curran, M. P. Dunphy, J. M. Simmie, C. K. Westbrook and W. J. Pitz, *Symp. Combust. Proc.*, 1992, **24**, 769-776.
23. H. Böhm, F. Baronnet and B. El Kadi, *Phys. Chem. Chem. Phys.*, 2000, **2**, 1929-1933.
24. A. Goldaniga, T. Faravelli, E. Ranzi, P. Dagaut and M. Cathonnet, *Symp. Combust. Proc.*, 1998, **27**, 353-360.
25. X. Fan, W. Sun, Z. Liu, Y. Gao, J. Yang, B. Yang and C. K. Law, *Proc. Combust. Inst.*, 2021, **38**, 321-328.
26. O. Staples, C. M. Moore, J. H. Leal, T. A. Semelsberger, C. S. McEnally, L. D. Pfefferle and A. D. Sutton, *Sustain. Energy Fuels*, 2018, **2**, 2742-2746.

27. K. W. Harrison and B. G. Harvey, *Sustain. Energy Fuels*, 2018, **2**, 367-371.
28. B. G. Harvey, W. W. Merriman and R. L. Quintana, *ChemSusChem*, 2016, **9**, 1814-1819.
29. A. Wildenberg, Y. Fenard, M. Carbonnier, A. Kéromnès, B. Lefort, Z. Serinyel, G. Dayma, L. Le Moyne, P. Dagaut and K. A. Heufer, *Proc. Combust. Inst.*, 2020, **38**, 543-553.
30. C. S. McEnally and L. D. Pfefferle, *Environ. Sci. Technol.*, 2011, **45**, 2498-2503.
31. P. C. St. John, S. Kim and R. L. McCormick, *Energy Fuels*, 2019, **33**, 10290-10296.
32. Y. Yang, A. L. Boehman and R. J. Santoro, *Combust. Flame*, 2007, **149**, 191-205.
33. ASTM, *ASTM D613-18ae1: Standard Test Method for Cetane Number of Diesel Fuel Oil*.
34. K. Cho, M. Han, C. S. Sluder, R. M. Wagner and G. K. Lilik, *SAE Tech. Pap.*, 2009, **2009-01-2669**.
35. L. Zheng, J. Cronly, E. Ubogu, I. Ahmed, Y. Zhang and B. Khandelwal, *Appl. Energy*, 2019, **238**, 1530-1542.
36. A. Torozova, P. Mäki-Arvela, A. Aho, N. Kumar, A. Smeds, M. Peurla, R. Sjöholm, I. Heinmaa, D. V. Korchagina and K. P. Volcho, *Journal of Molecular Catalysis A: Chemical*, 2015, **397**, 48-55.
37. D. L. Bartholet, M. A. Arellano-Treviño, F. L. Chan, S. Lucas, J. Zhu, P. C. S. John, T. L. Alleman, C. S. McEnally, L. D. Pfefferle and D. A. Ruddy, *Fuel*, 2021, **295**, 120509.
38. D. D. Das, C. S. McEnally, T. A. Kwan, J. B. Zimmerman, W. J. Cannella, C. J. Mueller and L. D. Pfefferle, *Fuel*, 2017, **197**, 445-458.
39. ASTM, *ASTM D975-20c: Standard Specification for Diesel Fuel*.
40. CEN, *CEN EN-590: Automotive Fuels-Diesel-Requirements and test methods*.
41. C. S. McEnally, D. D. Das and L. D. Pfefferle, *Yield Sooting Index Database Volume 2: Sooting Tendencies of a Wide Range of Fuel Compounds on a Unified Scale*, Harvard Dataverse, 2017.
42. J. Yanowitz, M. A. Ratcliff, R. L. McCormick, J. D. Taylor and M. J. Murphy, *Compendium of experimental cetane numbers*, National Renewable Energy Lab.(NREL), Golden, CO (United States), 2017.
43. ASTM, *ASTM D6890-18: Standard Test Method for Determination of Ignition Delay and Derived Cetane Number (DCN) of Diesel Fuel Oils by Combustion in a Constant Volume Chamber*.
44. G. Fioroni, L. Fouts, J. Luecke, D. Vardon, N. Huq, E. D. Christensen, X. Huo, T. L. Alleman, R. L. McCormick and M. D. Kass, *Society of Automotive Engineers Technical Paper Series*, 2019, **1**.
45. B. Ringner, S. Sunner and H. Watanabe, *Acta Chemica Scandinavica*, 1971, **25**, 141-146.
46. C. J. Mueller, W. J. Cannella, T. J. Bruno, B. Bunting, H. D. Dettman, J. A. Franz, M. L. Huber, M. Natarajan, W. J. Pitz and M. A. Ratcliff, *Energy Fuels*, 2012, **26**, 3284-3303.
47. K. Hackbarth, P. Haltenort, U. Arnold and J. Sauer, *Chemie Ingenieur Technik*, 2018, **90**, 1520-1528.
48. K. De Ras, M. Kusenberger, G. Vanhove, Y. Fenard, A. Eschenbacher, R. J. Varghese, J. Aerssens, R. Van de Vijver, L.-S. Tran and J. W. Thybaut, *Combust. Flame*, 2022, **238**, 111914.
49. N. Gaiser, H. Zhang, T. Bierkandt, S. Schmitt, J. Zinsmeister, T. Kathrotia, P. Hemberger, S. Shaqiri, T. Kasper and M. Aigner, *Combust. Flame*, 2022, 112060.
50. D. D. Das, W. J. Cannella, C. S. McEnally, C. J. Mueller and L. D. Pfefferle, *Proc. Combust. Inst.*, 2017, **36**, 871-879.
51. J. Luecke, M. J. Rahimi, B. T. Zigler and R. W. Grout, *Fuel*, 2020, **265**, 116929.
52. ASTM, *ASTM D8183-18: Standard Test Method for Determination of Indicated Cetane Number (ICN) of Diesel Fuel Oils using a Constant Volume Combustion Chamber-Reference Fuels Calibration Method*.
53. J. Luecke and B. T. Zigler, *Fuel*, 2021, **301**, 120969.
54. D. D. Das, P. C. S. John, C. S. McEnally, S. Kim and L. D. Pfefferle, *Combust. Flame*, 2018, **190**, 349-364.
55. C. S. McEnally and L. D. Pfefferle, *Combust. Flame*, 2007, **148**, 210-222.
56. B. D. Etz, G. M. Fioroni, R. A. Messerly, M. J. Rahimi, P. C. S. John, D. J. Robichaud, E. D. Christensen, B. P. Beekley, C. S. McEnally and L. D. Pfefferle, *Proc. Combust. Inst.*, 2021, **38**, 1327-1334.
57. Y. Kim, B. D. Etz, G. M. Fioroni, C. K. Hays, P. C. S. John, R. A. Messerly, S. Vyas, B. P. Beekley, F. Guo and C. S. McEnally, *Proc. Combust. Inst.*, 2021, **38**, 1143-1151.
58. M. S. Johnson, M. R. Nimlos, E. Ninnemann, A. Laich, G. M. Fioroni, D. Kang, L. Bu, D. Ranasinghe, S. Khanniche and S. S. Goldsborough, *Int. J. Chem. Kinet.*, 2021, **53**, 915-938.
59. J. T. Scanlon and D. E. Willis, *J. Chromatogr. Sci.*, 1985, **23**, 333-340.
60. M. J. Frisch, G. W. Trucks, H. B. Schlegel, G. E. Scuseria, M. A. Robb, J. R. Cheeseman, G. Scalmani, V. Barone, G. A. Petersson, H. Nakatsuji, X. Li, M. Caricato, A. V. Marenich, J. Bloino, B. G. Janesko, R. Gomperts, B. Mennucci, H. P. Hratchian, J. V. Ortiz, A. F. Izmaylov, J. L. Sonnenberg, Williams, F. Ding, F. Lipparini, F. Egidi, J. Goings, B. Peng, A. Petrone, T. Henderson, D. Ranasinghe, V. G. Zakrzewski, J. Gao, N. Rega, G. Zheng, W. Liang, M. Hada, M. Ehara, K. Toyota, R. Fukuda, J. Hasegawa, M. Ishida, T. Nakajima, Y. Honda, O. Kitao, H. Nakai, T. Vreven, K. Throssell, J. A. Montgomery Jr., J. E. Peralta, F. Ogliaro, M. J. Bearpark, J. J. Heyd, E. N. Brothers, K. N. Kudin, V. N. Staroverov, T. A. Keith, R. Kobayashi, J. Normand, K. Raghavachari, A. P. Rendell, J. C. Burant, S. S. Iyengar, J. Tomasi, M. Cossi, J. M. Millam, M. Klene, C. Adamo, R. Cammi, J. W. Ochterski, R. L. Martin, K. Morokuma, O. Farkas, J. B. Foresman and D. J. Fox, *Gaussian 16 Rev. C.01*, Wallingford, CT, 2016.
61. L. A. Curtiss, P. C. Redfern and K. Raghavachari, *J. Chem. Phys.*, 2007, **126**, 084108.
62. J. M. Simmie and K. P. Somers, *J. Phys. Chem. A*, 2015, **119**, 7235-7246.
63. K. P. Somers and J. M. Simmie, *J. Phys. Chem. A*, 2015, **119**, 8922-8933.
64. G. Luchini, J. V. Alegre-Requena, I. Funes-Ardoiz and R. S. Paton, *F1000Research*, 2020, **9**, 291.
65. Y.-P. Li, J. Gomes, S. Mallikarjun Sharada, A. T. Bell and M. Head-Gordon, *The Journal of Physical Chemistry C*, 2015, **119**, 1840-1850.
66. Y. Xuan and G. Blanquart, *Combust. Flame*, 2013, **160**, 1657-1666.
67. E. Kurtz, *Fuel properties to enable lifted-flame combustion*, Ford Motor Company, Dearborn, MI (United States), 2015.
68. J. A. Miller and S. J. Klippenstein, *J. Phys. Chem. A*, 2003, **107**, 7783-7799.
69. C. J. Pope and J. A. Miller, *Proc. Combust. Inst.*, 2000, **28**, 1519-1527.
70. W. Tang, R. S. Tranter and K. Brezinsky, *J. Phys. Chem. A*, 2006, **110**, 2165-2175.
71. M. Pelucchi, S. Namysl, E. Ranzi, A. Frassoldati, O. Herbinet, F.

- Battin-Leclerc and T. Faravelli, *Proc. Combust. Inst.*, 2019, **37**, 389-397.
72. N.-N. Wu, M.-Z. Zhang, S.-L. Ou-Yang and L. Li, *Molecules*, 2018, **23**, 1919.
73. Z. F. Xu, K. Xu and M. C. Lin, *ChemPhysChem*, 2009, **10**, 972-982.
74. H. Minwegen, U. Burke and K. A. Heufer, *Proc. Combust. Inst.*, 2017, **36**, 561-568.
75. C.-H. Wu, D. B. Magers, L. B. Harding, S. J. Klippenstein and W. D. Allen, *Journal of Chemical Theory and Computation*, 2020, **16**, 1511-1525.
76. E. Ranzi, M. Dente, A. Goldaniga, G. Bozzano and T. Faravelli, *Prog. Energy Combust.*, 2001, **27**, 99-139.
77. P. Dagaut, M. Cathonnet, M. McGuinness and J. M. Simmie, *Combust. Flame*, 1997, **110**, 409-417.
78. L. Li and P. B. Sunderland, *Combust. Sci. Technol.*, 2012, **184**, 829-841.
79. C. K. Westbrook, W. J. Pitz and H. J. Curran, *J. Phys. Chem. A*, 2006, **110**, 6912-6922.
80. R. D. Meininger, C.-B. M. Kweon, M. T. Szedlmayer, K. Q. Dang, N. B. Jackson, C. A. Lindsey, J. A. Gibson and R. H. Armstrong, *Int. J. Engine Res.*, 2017, **18**, 752-762.
81. P. C. S. John, Y. Guan, Y. Kim, S. Kim and R. S. Paton, *Nat. Commun.*, 2020, **11**, 1-12.
82. S. M. Villano, L. K. Huynh, H.-H. Carstensen and A. M. Dean, *J. Phys. Chem. A*, 2011, **115**, 13425-13442.
83. H. J. Curran, P. Gaffuri, W. J. Pitz and C. K. Westbrook, *Combust. Flame*, 1998, **114**, 149-177.
84. K. Hakimov, F. Arafin, K. Aljohani, K. Djebbi, E. Ninnemann, S. S. Vasu and A. Farooq, *Combust. Flame*, 2021, **223**, 98-109.
85. G. Issayev, S. M. Sarathy and A. Farooq, *Fuel*, 2020, **279**, 118553.
86. A. Miyoshi, *J. Phys. Chem. A*, 2011, **115**, 3301-3325.
87. A. Jalan, I. M. Alecu, R. Meana-Pañeda, J. Aguilera-Iparraguirre, K. R. Yang, S. S. Merchant, D. G. Truhlar and W. H. Green, *J. Am. Chem. Soc.*, 2013, **135**, 11100-11114.
88. Y. Fenard, A. Gil, G. Vanhove, H.-H. Carstensen, K. M. Van Geem, P. R. Westmoreland, O. Herbinet and F. Battin-Leclerc, *Combust. Flame*, 2018, **191**, 252-269.
89. X. Huo, N. A. Huq, J. Stunkel, N. S. Cleveland, A. K. Starace, A. E. Settle, A. M. York, R. S. Nelson, D. G. Brandner and L. Fouts, *Green Chem.*, 2019, **21**, 5813-5827.
90. J. Santner, F. M. Haas, F. L. Dryer and Y. Ju, *Proceedings of the Combustion Institute*, 2015, **35**, 687-694.
91. D. Splitter, R. Hanson, S. Kokjohn and R. D. Reitz, *SAE Tech. Pap.*, 2011, **2011-01-0363**.